

Design and Synthesis of Nanorod α -FeOOH@3DGF as Anode Material for Lithium-Ion Batteries with Enhanced Rate Performance and Cycle Stability

Wang Lianyang¹, Liu Liqiang¹, Zhang Chuangchuang¹, Wang Xin^{2,*}, Li Xingyi^{1,*}

¹ School of Materials Science and Engineering, Jiamusi University, Jiamusi 154007, PR China

² School of Materials Science and Engineering, Harbin University of Science and Technology, Harbin 150080, PR China

*E-mail: wanglianyangcl2017@163.com, 672346534@qq.com

Received: 3 January 2021 / Accepted: 12 April 2021 / Published: 30 April 2021

We designed and synthesized a new self-supporting composite with α -FeOOH nanorods and three-dimensional graphene foam (3DGF). When α -FeOOH is tightly combined with 3D graphene foam, it can maintain the microstructure of the electrode, and can effectively reduce the volume expansion and improve the cycle stability of the electrode. 3D graphene foam as a matrix material effectively improves the conductivity of the electrode material, providing a channel for rapid electron transfer. α -FeOOH@3DGF showed better lithium storage performance, and the reversible capacity remained at approximately 310 mAh·g⁻¹ after charging and discharging 100 cycles at 500 mA·g⁻¹.

Keywords: α -FeOOH@3DGF; Anode; Electrochemical characterization; Lithium-ion battery;

1. INTRODUCTION

Lithium-ion batteries are important electrochemical energy storage devices that have been widely used in portable mobile electronic devices, electric vehicles and aerospace applications. With the rapid development of electric vehicles, the requirements for the energy density, cycle life and cost of lithium-ion batteries has risen [1-3]. Developing battery materials with high energy density, low production cost and environmental friendliness to meet market and performance requirements has become the focus of scientific researchers. As a commercial anode material for lithium-ion batteries, the theoretical capacity of graphite is only 372 mAh·g⁻¹, which makes it difficult to meet high-power battery requirements in the future [4-6]. Therefore, developing a new anode material is an effective method of solving the above problems.

Among the many anode materials for lithium-ion batteries, α -FeOOH is abundant on earth, nontoxic, inexpensive and has attracted much attention due to its high specific capacity ($890 \text{ mAh}\cdot\text{g}^{-1}$) and good cycling performance [7,8]. It is considered to be a potential anode material. However, similar to other high specific capacity anode materials, α -FeOOH has the downside of exhibiting volume expansion during the charging and discharging cycles, resulting in a rapid decline in the electrode capacity [9-11]. Amine K [12] reported for the first time that β -FeOOH was used as an electrode material for lithium-ion batteries, and it showed excellent cycle stability. Tabuchi [11] reported that the capacity of β -FeOOH was maintained at $200 \text{ mAh}\cdot\text{g}^{-1}$ after 20 charging and discharging cycles at a voltage of 1.8V-4.0V. Recently, a large number of research results have shown that composite materials composed of electrode active materials and graphene can not only improve the conductivity of electrode materials, but can also improve the diffusion rate of electrons and ions in the electrode [5, 13-17]. FeOOH/graphene composite materials show excellent cycle stability and rate performance. However, it is still difficult to prepare FeOOH on a graphene matrix and improve the electrochemical performance of the composite system.

In this paper, based on the characteristics and advantages of α -FeOOH and graphene foam, we designed and synthesized a new self-supporting composite with α -FeOOH nanorods and 3D graphene foam (3DGF). A new type of α -FeOOH@3DGF was synthesized by a simple hydrothermal method.

2. EXPERIMENTAL

2.1 Synthesis of Graphene Foam (GF)

Three-dimensional graphene foam was prepared by chemical vapor deposition (CVD) using nickel foam as a template. A piece of nickel foam measuring $5 \text{ cm}\times 10 \text{ cm}$ was directly placed in a tubular furnace. The furnace was heated to $1000 \text{ }^\circ\text{C}$ and maintained for 10 min under an argon atmosphere to remove the thin layer of nickel foam oxides. Then, CH_4 , H_2 and Ar with flow rates of 50 SCCM, 100 SCCM and 800 SCCM were injected into the furnace. The furnace was heated for 10 min and then rapidly cooled to room temperature under a constant flow of Ar (500 SCCM) and H_2 (200 SCCM). A self-supporting three-dimensional graphene foam was prepared using nickel as the skeleton.

2.2 Synthesis of α -FeOOH@3DGF nanorods

The α -FeOOH@3DGF nanorods were obtained by a hydrothermal method. First, the 3D graphene foam was pretreated with nitric acid to remove the surface oxide layer. Then, 4 mmol $\text{FeCl}_3\cdot 6\text{H}_2\text{O}$ and 60 mmol urea were dissolved in 20 mL deionized water while magnetically stirring for 0.5 h. Afterwards, 1.5 mL of 37% hydrochloric acid was added to the above mixed solution and continuously stirred for 10 min to form a new uniform mixed solution. The mixed solution and 3D graphene foam were transferred to a 50 ml Teflon stainless steel autoclave, and the hydrothermal reaction was maintained at $150 \text{ }^\circ\text{C}$ for 15 h. Finally, the samples were washed three times with deionized water and ethanol.

3. RESULTS AND DISCUSSION

3.1 Microstructure and growth mechanism of rod α -FeOOH@3DGF

The XRD patterns of three-dimensional skeleton graphene (3DGF), the sample α -FeOOH and rod α -FeOOH@3DGF are shown in Fig. 1. As shown in Fig. 1(a), the XRD pattern of the growing matrix 3DGF shows that the diffraction peak can be calibrated by a standard card (PDF 98-000-0231). There was no other diffraction peaks except the diffraction peak of the standard card, meaning that the 3DGF matrix was very pure and did not contain any other impurities. The XRD patterns of rod-like α -FeOOH@3DGF and the sample α -FeOOH synthesized by the hydrothermal method are shown in Fig. 1 (b).

Fig. 1 shows that the diffraction peaks of the synthesized rod-shaped α -FeOOH@3DGF located at 33.4° , 34.5° , 35.6° , 39.6° , 46.8° and 56.5° corresponded to the (130), (021), (111), (121), (041) and (151) planes, respectively, according to the standard card (JCPDS No.: 34-1266) [20], which meant that the α -FeOOH phase had been synthesized by a hydrothermal reaction. Additionally, there were two obvious diffraction peaks at 26.5° and 54.5° assigned to 3DGF compared with the diffraction peaks of 3DGF in Fig. 1(a). In addition, there were no other obvious diffraction peaks except the diffraction peaks corresponding to α -FeOOH and 3DGF, indicating that no other phase was produced during the hydrothermal reaction. In comparison with the sample α -FeOOH, α -FeOOH@3DGF showed a larger half peak width of the diffraction peak with a smaller grain size, which was due to the presence of 3DGF in the hydrothermal reaction process; the 3DGF limited the grain growth to a certain extent.

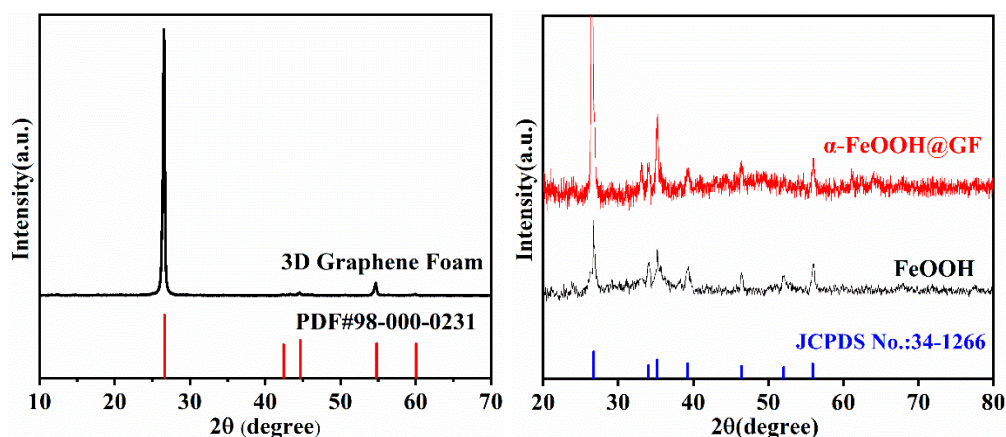


Figure 1. XRD patterns of 3DGF, α -FeOOH and α -FeOOH@3DGF (a) Graphene foam (b) Bare α -FeOOH and α -FeOOH@3DGF

To study the microstructure characteristics of the synthesized products, the morphology and structure of the rod like α -FeOOH@3DGF and α -FeOOH were characterized by SEM, as shown in Fig. 2. Fig. 2(a) and (b) showed the morphology characteristics of the matrix material 3DGF at different magnifications, which had a typical three-dimensional skeleton structure and relatively smooth surface. Meanwhile, when 3DGF was used as the growth matrix, the α -FeOOH@3DGF product obtained by the hydrothermal reaction displayed a typical nanorod structure, as shown in Fig. 2(c) and Fig. 2(d). In detail, the rod length was approximately 150-250 nm and the rod width was approximately 100 nm. The

morphology of the α -FeOOH without added 3DGF under the same hydrothermal conditions was shown in Fig. 2(e) and Fig. 2(f). It can be clearly seen from the figure that some rod-shaped α -FeOOH particles agglomerated together and formed larger aggregates.

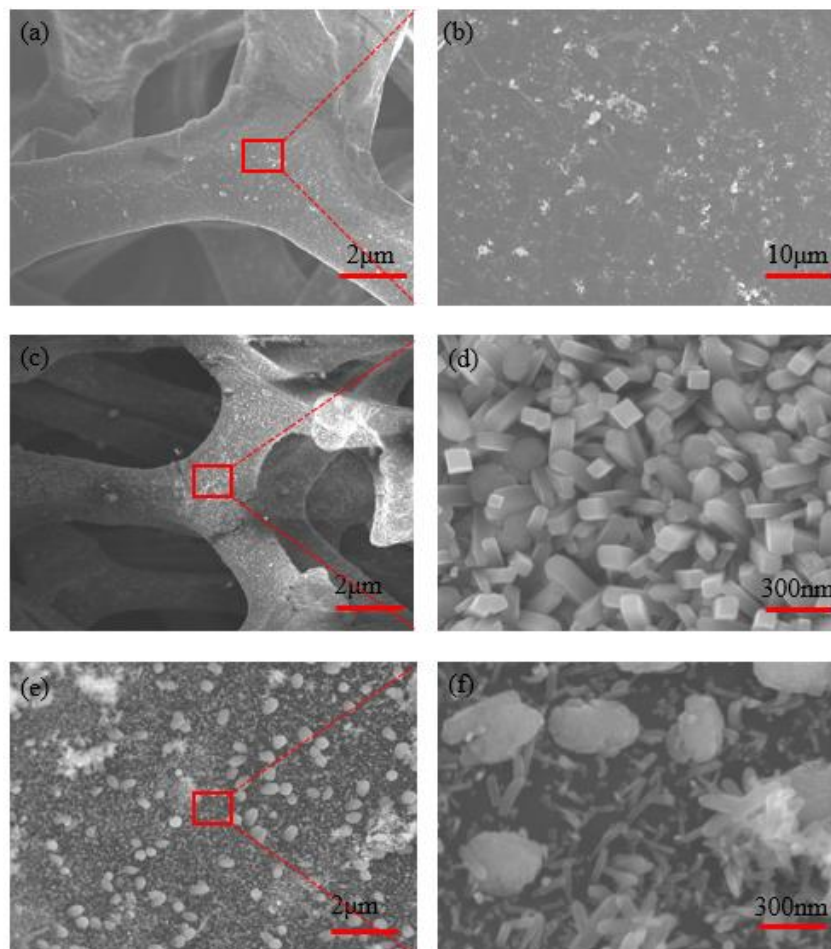


Figure 2. SEM image of different materials (a) graphene skeleton (b) amplification of graphene skeleton (c) nanorod α -FeOOH@3DGF (d) amplification of nanorod α -FeOOH@3DGF (e) bare α -FeOOH (f) amplification of bare α -FeOOH

The element distribution of rod like α -FeOOH@3DGF was analyzed by EDS, and the results were shown in Fig. 3. It can be seen in the figure that C, Fe and O were evenly distributed in the rod-like α -FeOOH@3DGF, indicating that α -FeOOH was successfully synthesized and that the element distribution was uniform.

The valence state and element composition of α -FeOOH@3DGF were evaluated by XPS, as shown in Fig. 4. Fig. 4(a) showed the full scan spectrum of rod-like α -FeOOH@3DGF containing Fe, O and C. Fig. 4(b) revealed the XPS spectra of Fe 2p. The clearly observed peaks at 709.2 eV and 723.1 eV corresponded to the Fe 2p_{3/2} and Fe 2p_{1/2}, respectively. In addition, satellite peaks were found around the main peaks, indicating the presence of Fe³⁺. Fig. 4(c) showed the XPS spectra of O 1s. The peak of O 1s can be divided into three peaks: Fe-O (527.9 eV), Fe-O-C (529.6 eV) and Fe-OH (530.1 eV). The

peak at 529.6 eV indicated the presence of Fe-O-C bonds between α -FeOOH and skeleton 3DGF. Fig. 4(d) showed the XPS spectra of C 1s. There were three valence bonds for C, as indicated by diffraction peaks at 288.6 eV, 284.5 eV and 282.8 eV. These three peaks correspond to C=O, C-O and C-C bonds; the C-O bonds might be the C-O-H, C-O-C and C-O-Fe bonds in the α -FeOOH@3DGF [18].

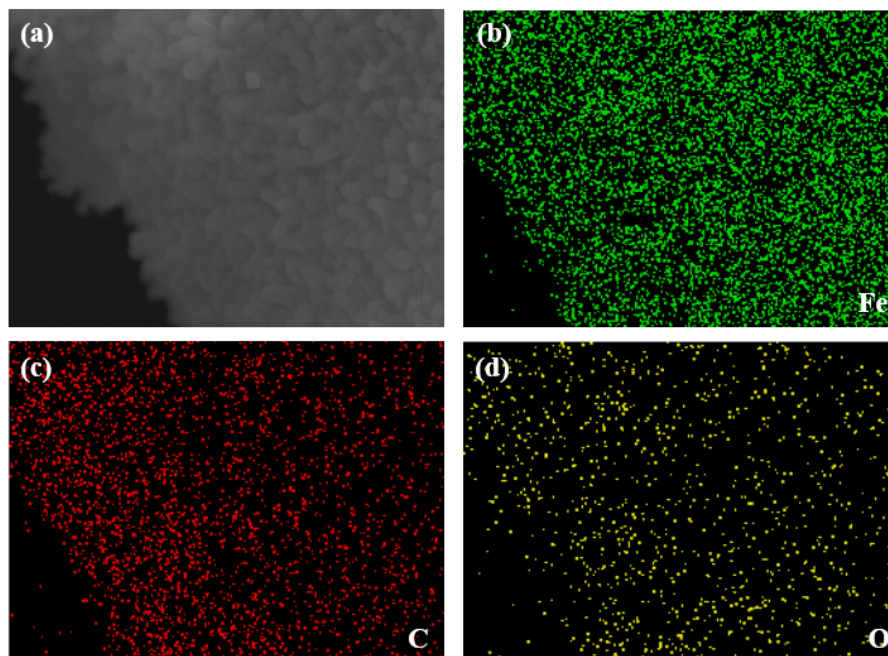


Figure 3. EDS elemental mapping of α -FeOOH@3DGF: (a) Morphology diagram, (b) C, (c) Fe, (d) O

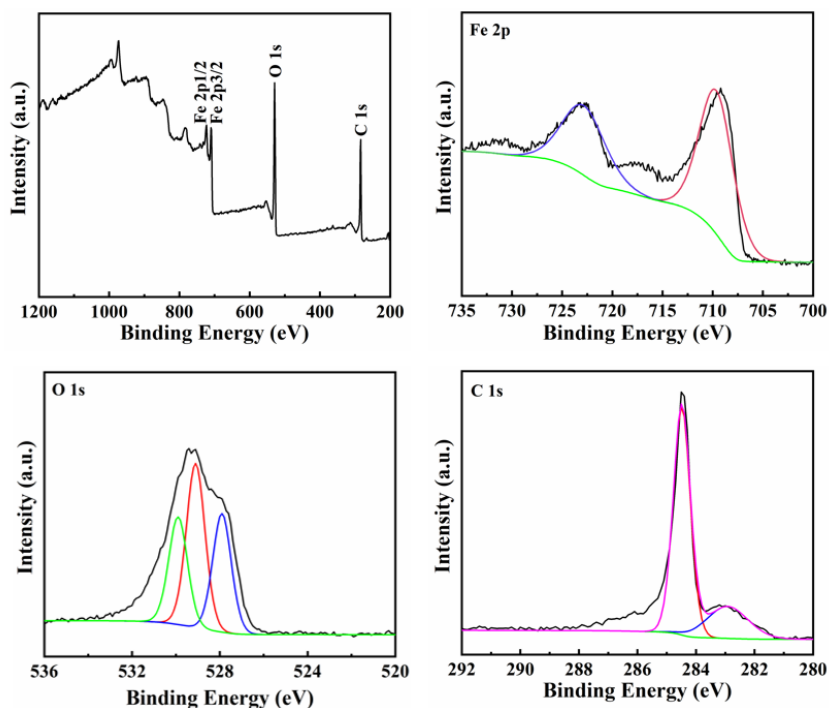


Figure 4. XPS survey spectra of α -FeOOH@3DGF: (a) survey spectrum, (b) Fe 2p, (c) O 1s, (d) C 1s

Thermogravimetric analysis (TGA) was performed to estimate the α -FeOOH content in the α -FeOOH@3DGF. Fig. 5 showed the TGA curves of α -FeOOH@3DGF and the sample α -FeOOH. It can be seen from the figure that the weight loss of the sample α -FeOOH material noticeably occurred when the heating temperature increased from 100°C to 400°C. The mass loss of α -FeOOH was 10.2% over the whole process. The main reason for the mass loss was that the iron(III) oxide-hydroxide transformed into iron oxide during heating, which was consistent with the theoretical weight loss of α -FeOOH (10%). However, there were two obvious weight loss peaks of α -FeOOH@3DGF in the curves. The weight loss that occurred during the heating stage from 100°C to 300°C was due to the decomposition of α -FeOOH into iron oxide and water, while the weight loss that occurred from 300°C to 500°C was mainly because of the oxidation of graphene to CO₂. The total mass was approximately 37.5% according to the calculation of the weight loss peaks, the content of 3DGF was approximately 23.4%, and the content of α -FeOOH in the composite was approximately 76.6%.

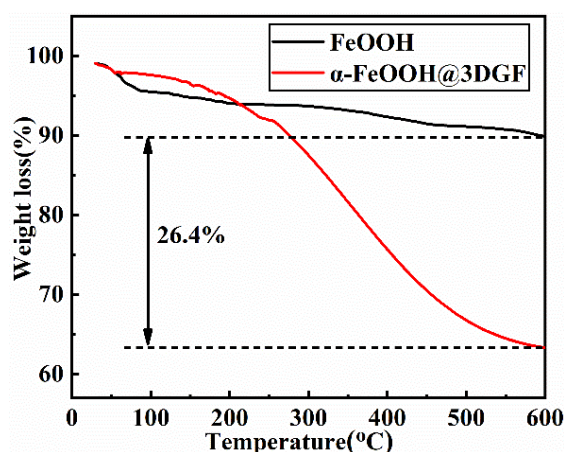


Figure 5. TGA analysis of α -FeOOH@3DGF and bare α -FeOOH

3.2. Electrochemical performance

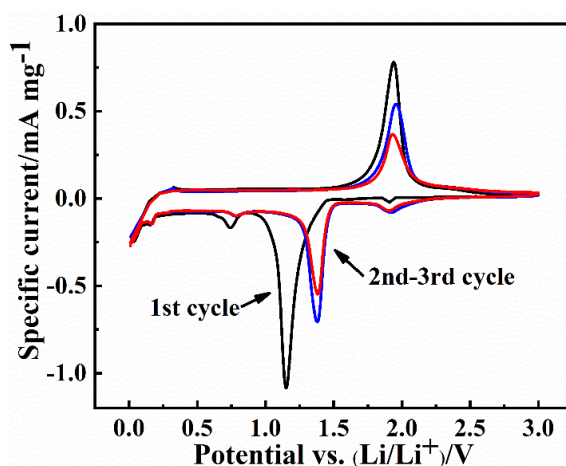


Figure 6. CV curve of α -FeOOH@3DGF at voltage window of 0.01-3.00 V at a scan rate of 0.1 mV·s⁻¹

Fig. 6 showed the first three charge-discharge CV curves of the α -FeOOH@3DGF in the voltage range of 0.01V-3.0 V at a scanning rate of $0.1 \text{ mV}\cdot\text{s}^{-1}$. As shown in Fig. 6, in the first cycle, reduction peaks and oxidation peaks can be clearly observed. The strong peak at 1.2 V corresponded to the formation of a solid electrolyte interlayer (SEI) [19], which disappeared during the following cycles. The peak at 1.42 V represented the oxidation of Li_2O to $\text{Li}_{1+x}\text{FeOOH}$ [21]. During the cycles that followed, the similar CV curves indicated the better cycle stability of α -FeOOH@3DGF.

Fig. 7 showed the charging and discharging curves of the rod-like α -FeOOH@3DGF and the sample α -FeOOH with a voltage of 0.3 V-3.0 V for the first, second and third cycles. As shown in Fig. 7(a), the rod-like α -FeOOH@3DGF, experienced a noticeable voltage plateau in the first discharging cycle. The plateau at 0.75 V indicated that the electrode material was reduced to Fe^0 and a solid electrolyte interlayer (SEI) was formed. However, no voltage plateau at 0.75 V was observed in the following discharging curve, indicating that this reaction was partially irreversible during the charging-discharging cycle. There was no other obvious plateau in the discharge cycle in any curve except the one described above, indicating the excellent reversibility of the α -FeOOH@3DGF during the charging and discharging process. The first charging capacity and discharging capacity of the α -FeOOH@3DGF were $355 \text{ mAh}\cdot\text{g}^{-1}$ and $448 \text{ mAh}\cdot\text{g}^{-1}$, respectively, with a coulomb efficiency of 79.2%. The charging and discharging curves in the second and third cycles were similar, indicating a stable state. Fig. 7(b) showed the charging and discharging curves of the first, second and third cycles of the sample α -FeOOH. As shown in Fig. 7(b), the discharging capacity was only $165 \text{ mAh}\cdot\text{g}^{-1}$ at 3 cycles, indicating a very obvious irreversible decline and poor cycle performance.

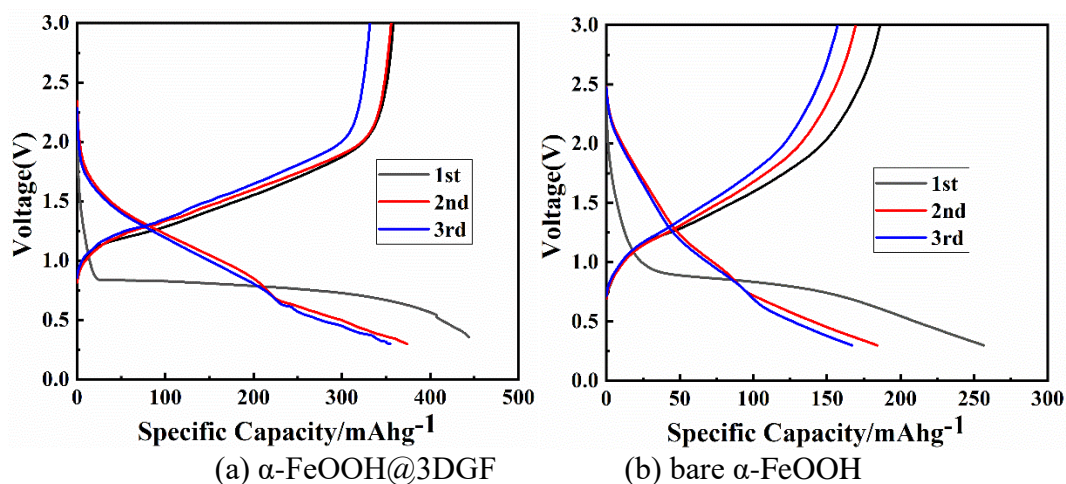


Figure 7. Charge-discharge profiles of α -FeOOH@3DGF and α -FeOOH of $500 \text{ mA}\cdot\text{g}^{-1}$ for different cycles

To determine the cycle stability, the rod-like α -FeOOH@3DGF and the sample α -FeOOH were tested at a current density of $500 \text{ mA}\cdot\text{g}^{-1}$. As shown in Fig. 8, the first discharging capacity and first charging capacity of α -FeOOH@3DGF were $685 \text{ mAh}\cdot\text{g}^{-1}$ and $515 \text{ mAh}\cdot\text{g}^{-1}$, respectively. After more than ten charging and discharging cycles, the coulombic efficiency was almost 100%, with a stable capacity of approximately $410 \text{ mAh}\cdot\text{g}^{-1}$. After 200 charging and discharging cycles, the reversible capacity remained at approximately $345 \text{ mAh}\cdot\text{g}^{-1}$, indicating good cycle stability. However, the first

discharging capacity and first charging capacity of the α -FeOOH were 686 mAh·g⁻¹ and 512 mAh·g⁻¹, respectively, which were lower than those of rod α -FeOOH@3DGF. The reversible capacity of α -FeOOH decreased to 200 mAh·g⁻¹ after only 20 cycles, and then remained at only 120 mAh·g⁻¹, indicating poor cycle performance. In total, it was obvious that the capacities of α -FeOOH@3DGF and α -FeOOH experienced different degrees of irreversible loss during the first 10 cycles. After 20 cycles, both basically reached a relatively stable state. However, the capacity of the rod-like α -FeOOH@3DGF was much higher than that of the α -FeOOH, mainly because the three-dimensional graphene matrix of α -FeOOH@3DGF stabilized the structure. The three-dimensional graphene matrix prevented the collapse and pulverization of the rod-shaped α -FeOOH and stabilized the electrode microstructure, which was conducive to the transmission and movement of electrons and ions. The results showed that the reversible capacity of α -FeOOH were significantly improved by coupling α -FeOOH with 3D graphene, and the structural stability and cycle stability of the electrode materials were also enhanced.

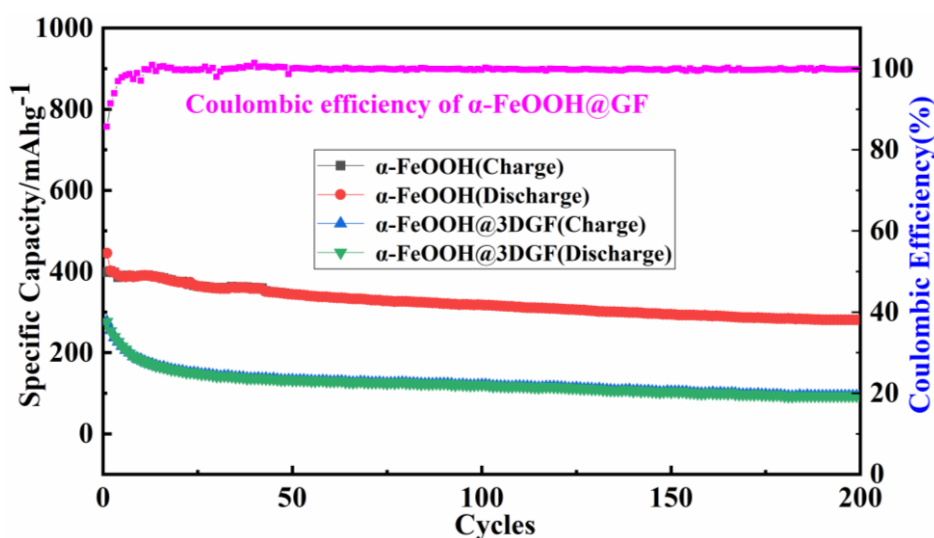


Figure 8. Cycling performance of α -FeOOH@3DGF and α -FeOOH at a current density of 500 mA·g⁻¹

The rate performances of rod-like α -FeOOH@3DGF and α -FeOOH were tested at different current densities of 0.1 A·g⁻¹, 0.2 A·g⁻¹, 0.5 A·g⁻¹, 1 A·g⁻¹ and 0.1 A·g⁻¹. The rod-like α -FeOOH@3DGF exhibited stable and high capacity at different current densities, as shown in Fig. 9, with reversible capacities 724.5 mAh·g⁻¹, 498.4 mAh·g⁻¹, 306.9 mAh·g⁻¹, 223.1 mAh·g⁻¹ and 623.2 mAh·g⁻¹. However, the α -FeOOH exhibited a low capacity of approximately 385.5 mAh·g⁻¹, 218.2 mAh·g⁻¹, 116.9 mAh·g⁻¹, 63.1 mAh·g⁻¹ and 208.6 mAh·g⁻¹. By comparison, it was found that when the current density was restored to 0.1 A·g⁻¹, the capacity could still return to 648 mAh·g⁻¹ after experiencing different current densities and multiple charging-discharging cycles. This evidence implied that the microstructure of the α -FeOOH@3DGF had not been damaged and could still work stably while undergoing a large amount of current charging and discharging. According to the above comparative analysis, the main reason for the better rate performance of the α -FeOOH@3DGF was that matrix α -FeOOH could be combined well with a three-dimensional graphene framework. Strong binding more easily maintained the three-

dimensional skeleton structure, which was favorable for electron and ion transmission and volume expansion relief. Therefore, compared with the control sample α -FeOOH, α -FeOOH@3DGF had a better rate performance. Additionally, the results of this paper were compared with the results of the existing literature, as shown in Table 1. Table 1 showed that the α -FeOOH@3DGF has good cycle stability and rate performance.

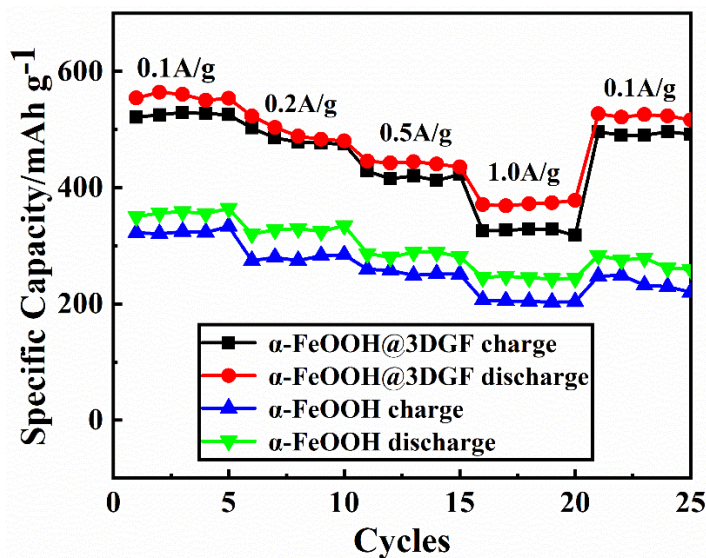


Figure 9. Rate performance of α -FeOOH@3DGF and α -FeOOH

Table 1. Recent progress on material synthesis and electrochemical performance of α -FeOOH batteries

Materials	Voltage range (V vs Li ⁺ /Li)	Cycling data	Rate capability	Ref.
amorphous FeOOH	1.5-4.0	110/100th/200 mA·g ⁻¹	-	[4]
β -FeOOH/Ti ₃ C ₂	0.05-3.0	300/200th/200 mA·g ⁻¹	233/1 A·g ⁻¹	[7]
β -FeOOH thin film	1.8-3.0	135/20th/0.05 C	165/10 C	[11]
α -FeOOH	0.01-3.0	155/200th/500 mA·g ⁻¹	143/1 A·g ⁻¹	This paper
α -FeOOH@3DGF	0.01-3.0	293/200th/500 mA·g ⁻¹	252/1 A·g ⁻¹	This paper

To further study the chemical reaction kinetics, electrochemical impedance spectroscopy (EIS) was used to further test the sodium storage properties of rod-like α -FeOOH@3DGF. Fig. 10 displayed the Nyquist plots of rod-like α -FeOOH@3DGF and α -FeOOH. As can be clearly seen from the figure, the diameter of the semicircle in the high-frequency region of the rod-like α -FeOOH@3DGF was smaller than that of the α -FeOOH. The radius of the high-frequency region represented the impedance of the charging, implying that the rod-like α -FeOOH@3DGF had little impedance and fast transmission. This rapid transmission made it easier for Li⁺ to react on the electrode surface and interface, which was more

conductive to improving the rate of the electrochemical reaction and the specific capacity of electrode materials [22].

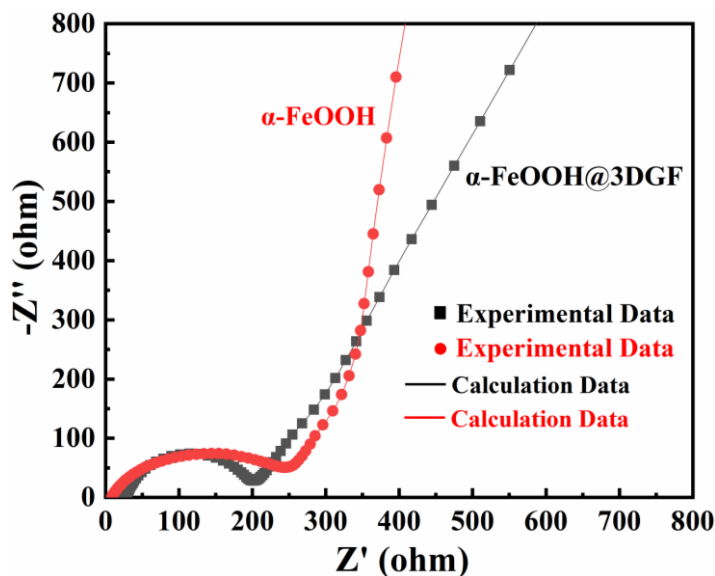


Figure 10. Electrochemical impedance spectra (EIS) of α -FeOOH@3DGF and bare α -FeOOH

4. CONCLUSION

This paper reports the successful hydrothermal synthesis of a rod-like α -FeOOH@3DGF material with length of 1 μm and width of 200 nm. The α -FeOOH@3DGF showed better lithium storage performance, and the reversible capacity remained at approximately $310 \text{ mAh}\cdot\text{g}^{-1}$ after 100 charging and discharging cycles at $500 \text{ mA}\cdot\text{g}^{-1}$. The combination of rod-shaped α -FeOOH and a three-dimensional graphene structure can effectively ensure a stable microstructure, which is conducive to improving the cycle stability and rate performance of the electrode.

The main reasons for the good cycle performance of α -FeOOH@3DGF are as follows: The three-dimensional graphene as a matrix material effectively improved the conductivity of the electrode, providing a channel for rapid electron transfer. This increase in conductivity can effectively reduce the electron transfer impedance and improve the capacity of the electrode. In addition, when three-dimensional graphene is tightly combined with α -FeOOH, the microstructure of the electrode can be well maintained, which can effectively reduce the volume expansion and improve the cycle stability of the electrode.

ACKNOWLEDGEMENTS

National Natural Science Foundation of China (51875252, 51804091), Harbin Applied Technology Research and Development Project (2017RAQXJ009).

References

1. J. B. Goodenough and Y. Kim, *Chem. Mater.*, 22 (2010) 587.

2. Z.M. Zheng, Y. Zao, Q.B. Zhang, Y. Cheng, H.X. Chen, K.L. Zhang, M.S. Wang and D.L. Peng, *Chem. Eng. J.*, 347 (2018) 563.
3. B. Scrosati and J. Garche, *J. Power Sources*, 195 (2010) 2419.
4. H. Morimoto, K. Takeno, Y. Uozumi, K. Sugimoto and S. Tobishima, *J. Power Sources*, 196 (2011) 6512.
5. G. Zhang, Y. Shi, H. Wang, L. Jiang, X. Yu, S. Jing, S. Xing and P. Tsiakaras, *J. Power Sources*, 416 (2019) 118.
6. X. Zhu, Y. Zhu, S. Murali, M. D. Stoller and S. R. Ruoff, *ACS Nano*, 5 (2011) 3333.
7. C. Xue, Y. He, Y. Liu, P. Saha and Q. Cheng, *Ionics*, 25 (2019) 3069.
8. I. Muhammad, Z.X. Chen, C. L. Zhu, P. Hui, Z. Imran, L. Yao, W. B. Syeda. R. Y. Luan, N. Salma and S. M. Zhu, *Electrochim. Acta*, 283 (2018) 401.
9. L. Yu, C. Wei, Q. Yan and Z. Xu, *Nano Energy*, 13 (2015) 397.
10. F. Zhou, X. Zhao, C. Yuan and H. Xu, *Chem. Lett.*, 35 (2006) 1410.
11. T. Tabuchi, Y. Katayama, T. Nukuda and Z. Ogumi, *J. Power Sources*, 191 (2009) 640.
12. K. Amine, H. Yasuda and M. Yamachi, *J. Power Sources*, 81 (1999) 221.
13. L. Dan, *ACS Appl. Mater.*, 26 (2018) 22841.
14. K. Xi, P. R. Kidambi, R. Chen, C. Gao and X. Peng, *Nanoscale*, 6 (2014) 5746.
15. Y. Zhu, S. Murali, M. D. Stoller, K. J. Ganesh, W. Cai, P. J. Ferreira, A. Pirkle, R. M. Wallace, K. A. Cychoz and M. Thommes, *Science*, 332 (2011) 1537.
16. G. Wu, J. Chen, Y. Guo, X. Li, B. Luo, L. Chu, Y. Han, B. Jiang and L. Xu, *J. Electrochem. Soc.*, 164 (2017) 3060.
17. X. Zhang and Y. Du, *RSC Adv.*, 6 (2016) 17504.
18. S. Stankovich, R. D. Piner, X. Q. Chen, N. Q. Wu, S. T. Nguyen and R. S. Ruoff, *J. Mater. Chem.*, 16 (2006) 155.
19. J. Maier, *Nat. Mater.*, 4 (2005) 805.
20. X. Wang, X. Chen, L. Gao, H. Zheng, M. Ji, C. Tang, T. Shen and Z. Zhang, *J. Mater. Chem.*, 14 (2004) 905.
21. H. Qi, L. Cao, J. Li, J. Huang, Z. Xu, Y. Cheng, K. Yanagisawa, *ACS Appl. Mater.*, 8 (2016) 35253.
22. B. Ahmed, D. H. Anjum, Y. Gogotsi and H. N. Alshareef, *Nano Energy*, 34 (2017) 249.